On the Necessary Grid Resolution for Verified Calculation of Premixed Laminar Flames

Ashraf N. Al-Khateeb, Joseph M. Powers* and Samuel Paolucci

Department of Aerospace and Mechanical Engineering, University of Notre Dame, Notre Dame, Indiana 46556-5637, USA.

Abstract. We consider the grid resolution necessary to resolve combustion in a mixture of calorically imperfect ideal gases described by detailed kinetics and multicomponent transport. Using the steady premixed laminar flame as a paradigm, the required spatial discretization to capture all detailed physics in the reaction zone is found via 1) determination of the finest grid used in a standard software tool which employs adaptive mesh refinement, 2) examination of peak values of intermediate species mass fractions in the flame zone as a function of grid size, 3) a formal grid resolution study, and 4) a robust new eigenvalue analysis developed to estimate the finest length scale. Application to laminar premixed flames in hydrogen-air flames reveals that the finest length scale is on the order of 10^{-4} cm for combustion at atmospheric pressure. Resolution at this scale is shown to be necessary to capture detailed species mass fraction profiles; other features such as steady flame speeds and equilibrium thermochemical properties do not have such a stringent length scale requirement.

1 Introduction

Here we will employ a few basic numerical strategies to develop reliable tools which can give estimates of the grid size necessary for a mathematically verified calculation of reacting flows. The estimates are developed for a simple configuration: a one-dimensional steady laminar flame. Indeed, it may come as a surprise that such straightforward tools as grid convergence studies of laminar flames have not been highlighted in the literature.

---

*Corresponding author. *Email addresses:* `aalkhate@gmail.com` (A. N. Al-Khateeb), `powers@nd.edu` (J. M. Powers), `paolucci@nd.edu` (S. Paolucci)

But that is in fact the *status quo*, and the absence of such studies, coupled with the ultimate need for accurate reacting flow calculations for more complex scenarios, justifies the straightforward exercise presented here.

There is some ambiguity in the combustion literature about what constitutes a resolved solution. Many consider a calculation to be resolved if certain global or derived quantities, such as steady flame speed, are insensitive to grid size. Indeed, these are necessary conditions. However, as discussed by Roache [1], convergence of only global quantities is not a sufficient indicator of a fully resolved solution, and taken alone can lead to incorrect conclusions. While a derived quantity may be a function of all dependent variables, it may be insensitive to errors in some of them. Which variables they are insensitive to is problem-dependent, and impossible to determine *a priori*. In the context of a combustion problem, the fact that one may be using a grid which captures the correct flame speed offers no guarantee that species mass fractions have been accurately predicted.

Here, we follow Roache [1] and adopt the more rigorous characterization of a resolved solution as one in which *all dependent variables throughout the domain* are insensitive to changes in discretization size. This more demanding characterization is fully consistent with standard notions found in the broader mathematical and scientific computing literature, cf. [2–6]. The exercise of demonstrating the harmony of the discrete solution with the foundational mathematics is known as verification [7]. Neglecting this issue can give rise to solutions whose macro-behavior depends on the size of the grid and the algorithm that has been used to solve the mathematical model.

For multi-scale problems, verification is difficult due to the range of the scales, which may span many orders of magnitude. Nonlinearity can induce significant coupling across the scales so that errors at small scales can rapidly cascade to the large scales. Moreover, the strength of the coupling across the scales is not known *a priori*. So, all the physical scales of the mathematical model have to be captured in order to have full confidence that predictions are repeatable, grid-independent, and thus verifiable. The main aim of this paper is to estimate the required spatial resolution to capture all physical scales in a standard multi-scale problem: the steady one-dimensional laminar premixed flame propagating freely at atmospheric pressure in a stoichiometric mixture of hydrogen-air described by detailed kinetics and multi-component transport.

In a complementary study, two of the authors [8] gave a robust method to provide an accurate determination of the finest length scale in the reaction zone of a Chapman-Jouguet detonation based on spatial eigenvalue analysis. It was concluded that the required spatial discretization for detonations in hydrogen-air mixtures initially at atmospheric pressure is $\sim 10^{-4}$ cm. Here, the method employed in [8] to calculate the length scales for gas phase detonation is implemented with modification for deflagration. The method is reliable in that it has little dependence on the details of the underlying numerical method used to calculate the laminar flame. It simply requires a local determination of the state of the system. As such, it is able to estimate accurately the length scales using a fundamental mathematical approach. Lastly, the present study extends some of our

preliminary work on laminar flames [9, 10].

The paper is organized as follows. In Section 2, the governing partial differential equations (PDEs) for unsteady reactive flow are presented. These are reduced into a system of differential algebraic equations (DAEs) which describes the spatial evolution of the state variables. In this section we also describe the numerical algorithm. In Section 3, results are given. In Section 3.1, the algorithm is verified by comparison with calculations given by Smooke *et al.* [11] for a laminar premixed flame in a hydrogen-air mixture using a standard adaptive refinement method. On a related problem, we then give a simple estimate of the necessary grid resolution by examining the finest grid size employed by the adaptive method. Then in Section 3.2 we use simulations on several uniform grids to see how a challenging intermediate species mass fraction's peak value converges within the flame zone. Next, in Section 3.3, a more rigorous verification is given by a grid convergence study to demonstrate the necessary and sufficient discretization size required to guarantee that the prediction of dependent variables throughout the domain is insensitive to grid size. Lastly in Section 3.4, all the length scales predicted by the corresponding spatial eigenvalue problem are shown, and the finest length scale is compared with the flame thickness. This comparison is presented for a wide range of pressures.

2 Mathematical model

2.1 Governing equations

The following unsteady equations, in conservative form, describe the system under consideration: a one-dimensional adiabatic laminar premixed mixture of N molecular species composed of L atomic elements which undergo J reversible reactions [12, 13] with no body force:

$$\frac{\partial \rho}{\partial \tilde{t}} = -\frac{\partial}{\partial \tilde{x}}(\rho \tilde{u}), \tag{2.1}$$

$$\frac{\partial}{\partial \tilde{t}}(\rho \tilde{u}) = -\frac{\partial}{\partial \tilde{x}}(\rho \tilde{u}^2 + p - \tau), \tag{2.2}$$

$$\frac{\partial}{\partial \tilde{t}}\left(\rho\left(e + \frac{\tilde{u}^2}{2}\right)\right) = -\frac{\partial}{\partial \tilde{x}}\left(\rho \tilde{u}\left(e + \frac{\tilde{u}^2}{2} + \frac{p}{\rho} - \frac{\tau}{\rho}\right) + J^q\right), \tag{2.3}$$

$$\frac{\partial}{\partial \tilde{t}}(\rho Y_i) = -\frac{\partial}{\partial \tilde{x}}(\rho \tilde{u} Y_i + J_i^m) + \dot{\omega}_i M_i, \quad 1 \leq i \leq N-1. \tag{2.4}$$

Here, we use the tilde to denote the laboratory reference frame. The independent variables are the spatial coordinate $\tilde{x}$ and time $\tilde{t}$. The dependent variables are mixture density ρ, mixture velocity $\tilde{u}$, mixture pressure p, mixture viscous stress τ, mass-based specific internal energy of the mixture e, total heat flux J^q, and for the ith specie, Y_i, J_i^m, and $\dot{\omega}_i$, which are the mass fraction, the diffusive mass flux, and the molar production rate per unit volume, respectively. The constant M_i is the molecular mass of specie i. Eqs. (2.1)-(2.3)

describe the conservation of mass, linear momentum, and energy, respectively. Eq. (2.4) is an evolution equation for $N-1$ species. This system of equations is completed by adopting a standard set of constitutive equations for an ideal mixture of reacting calorically imperfect ideal gases. The mixture is taken to react according to the law of mass action for detailed chemical kinetics with Arrhenius temperature-dependency. For diffusive momentum and energy transport, appropriate mixture diffusivity coefficients are adopted; for diffusive mass-transport a multi-component diffusion model is employed. Details are found in Appendix A.1.

The complete system is simplified to the following form which commonly appears in the literature to model stationary laminar premixed flames at constant pressure and low Mach number, cf. [14–17]:

$$\frac{d}{dx}(\rho u)=0, \tag{2.5}$$

$$\rho u c_p \frac{dT}{dx}+\frac{dq}{dx}+\sum_{i=1}^{N}\left(J_i^m\frac{dh_i}{dx}+\dot{\omega}_i M_i h_i\right)=0, \tag{2.6}$$

$$\rho u \frac{dY_i}{dx}+\frac{dJ_i^m}{dx}=\dot{\omega}_i M_i, \quad 1\le i\le N-1. \tag{2.7}$$

Here x and u are the distance coordinate and fluid particle velocity, respectively, measured in the reference frame in which the flame is stationary, c_p is the mixture-averaged specific heat at constant pressure, T is the temperature, q is the Fourier heat flux, and h_i is the enthalpy of specie i. These are completed with an appropriate set of boundary conditions:

$$x=0: \quad T=T_o, \quad Y_i+\frac{J_i^m}{\rho_o S}=Y_{io}, \quad 1\le i\le N-1, \tag{2.8}$$

$$x\to\infty: \quad \frac{dT}{dx}\to 0, \quad \frac{dY_i}{dx}\to 0, \quad 1\le i\le N-1, \tag{2.9}$$

$$x=x_f: \quad T=T_f, \tag{2.10}$$

where S is the flame speed, x_f is a specified spatial point and T_f is the specified temperature at that location [15]. These are commonly used to study deflagration, though other formulations are possible. These boundary conditions are sufficient for freely propagating flames, where for this type of flame the mass flow rate is unknown [16, 17], so the temperature at an interior spatial point has to be specified. The point x_f and temperature T_f have to be selected such that all the gradients approach zero at the cold boundary at $x=0$. A detailed reduction of Eqs. (2.1)-(2.4) to Eqs. (2.5)-(2.7) is given in Appendix A.2.

A solution for the boundary value problem with the boundary conditions can be obtained by discretizing the spatial domain using finite differences. The resulting algebraic system of equations is then solved iteratively using a damped modified Newton's method, where the solution iterate is brought into the convergence domain by using pseudo-time integration [14]. We will use this method for our steady flame calculations.

In all cases the iterative errors we obtain correspond to a relative tolerance RTOL=10^{-9} and absolute tolerance ATOL=10^{-14}, as defined in detail in [14]. The values utilized are five orders of magnitude more stringent than the default values; moreover, the absolute tolerance is approaching the machine precision error.

The standard form of Eqs. (2.5)-(2.7) is inconvenient for a rigorous eigen-analysis of the length scales. For this task, a non-traditional system of DAEs is more convenient. Following lengthy analysis, one obtains the system of DAEs:

$$\mathbf{A}(\mathbf{z}) \cdot \frac{d\mathbf{z}}{dx} = \mathbf{f}(\mathbf{z}). \tag{2.11}$$

Appendix A.2 gives details of the reduction to Eq. (2.11). Here $\mathbf{z}$ is a set of state variables, $\mathbf{A}$ is a singular matrix, and $\mathbf{f}$ is a set of forcing functions; see Eqs. (A.26)-(A.27).

2.2   A posteriori length scale analysis

To accurately determine the length scales over which the system evolves, an eigenvalue analysis of Eq. (2.11) can be performed. Since $\mathbf{A}$ is singular, standard eigenvalue analysis is not applicable. Instead, the generalized eigenvalues of this dynamical system are calculated [18]. Employing the generalized eigenvalue method on a singular system is a robust method to distinguish small physically based eigenvalues from those which are mathematically zero. This is particularly important in multi-scale problems where ordinary eigenvalue analysis often generates a set of eigenvalues for which the distinction is either difficult or impossible. The mathematical zero eigenvalues arise from the invariants of the problem.

Assume first that $\mathbf{z} = \widehat{\mathbf{z}}(x)$ has been determined by some appropriate numerical method so that $\widehat{\mathbf{z}}(x)$ satisfies Eqs. (2.5)-(2.10) (and thus also Eq. (2.11)). Consider then an arbitrary spatial point $x = x^*$ at which the state variables are $\mathbf{z} = \widehat{\mathbf{z}}(x^*) = \mathbf{z}^*$. By defining the perturbation from $\widehat{\mathbf{z}}(x)$ as $\mathbf{z}'(x) = \mathbf{z}(x) - \widehat{\mathbf{z}}(x)$, and linearizing Eq. (2.11) about $x = x^*$, one finds

$$\left(\mathbf{A}^* + \mathbf{\Psi}^* \cdot \mathbf{z}' + \mathcal{O}\left(\mathbf{z}'^2\right) + \cdots\right) \cdot \left(\left.\frac{d\widehat{\mathbf{z}}}{dx}\right|_{x=x^*} + \frac{d\mathbf{z}'}{dx}\right) = \left(\mathbf{f}^* + \mathbf{J}^* \cdot \mathbf{z}' + \mathcal{O}\left(\mathbf{z}'^2\right) + \cdots\right), \tag{2.12}$$

where $\mathbf{A}^* = \mathbf{A}(\mathbf{z}^*)$, $\mathbf{f}^* = \mathbf{f}(\mathbf{z}^*)$ are now locally constant, $\mathbf{J}^*$ is the locally constant Jacobian evaluated as

$$J_{ik}^* = \left.\frac{\partial f_i}{\partial z_k}\right|_{\mathbf{z}=\mathbf{z}^*}, \quad 1 \leq i,k \leq 2N+2, \tag{2.13}$$

and $\mathbf{\Psi}^*$ is a locally constant third-order matrix given by

$$\Psi_{ijk}^* = \left.\frac{\partial A_{ij}}{\partial z_k}\right|_{\mathbf{z}=\mathbf{z}^*}, \quad 1 \leq i,j,k \leq 2N+2. \tag{2.14}$$

By considering only linear terms in Eq. (2.12) and employing the fact that $\mathbf{A}^* \cdot d\widehat{\mathbf{z}}/dx|_{x=x^*} = \mathbf{f}^*$, one finds that

$$\mathbf{A}^* \cdot \frac{d\mathbf{z}'}{dx} = \mathbf{J}^* \cdot \mathbf{z}' - \mathbf{\Psi}^* \cdot \mathbf{z}' \cdot \frac{d\widehat{\mathbf{z}}}{dx}\bigg|_{x=x^*}, \tag{2.15}$$

which can be compactly rewritten as

$$\mathbf{A}^* \cdot \frac{d\mathbf{z}'}{dx} = \mathbf{B}^* \cdot \mathbf{z}', \tag{2.16}$$

where

$$B_{ik}^* = \left(J_{ik}^* - \Psi_{ijk}^* \frac{d\widehat{z}_j}{dx}\bigg|_{x=x^*} \right), \quad 1 \leq i,k \leq 2N+2. \tag{2.17}$$

Next, adopt the standard assumption that

$$\mathbf{z}' = e^{\lambda x}\mathbf{v}, \tag{2.18}$$

where λ and $\mathbf{v}$ are constants to be determined. Substitution of Eq. (2.18) into Eq. (2.16) yields the generalized eigenvalue problem

$$\lambda \mathbf{A}^* \cdot \mathbf{v} = \mathbf{B}^* \cdot \mathbf{v}, \tag{2.19}$$

where λ is in general a complex number denoting the generalized eigenvalue, and $\mathbf{v}$ is the corresponding generalized eigenvector. Solving for λ_i, $i = 1, \cdots, 2N-L$, then from Eq. (2.18) it is easily seen that the length scales over which the perturbations evolve are given by the reciprocal of the real part of these eigenvalues,

$$\ell_i = \frac{1}{|Re(\lambda_i)|}, \quad 1 \leq i \leq 2N-L. \tag{2.20}$$

In general, the eigenvalues are complex, where the reciprocals of the real parts provide the length scales of amplitude growth, and the reciprocals of the imaginary parts represent the oscillatory length scale. In this work, the eigenvalues are purely real, except in some limited portions of the domain. By evaluating the eigenvalues at each spatial point, the length scales over which the system evolves are determined. As a result, the minimum size of discretization to capture the finest scale of the system can be determined. We note that this minimum scale is not necessarily required everywhere in the domain. However, this might justify the use of spatially adaptive algorithms.

2.3 Computational method for spatial eigenvalues

A double precision FORTRAN-77 code has been developed and linked with the International Mathematical and Statistical Libraries (IMSL) routines DFDJAC for Jacobian evaluation, DGVLRG for generalized eigenvalues estimation, and a double precision version

of the public domain edition of the CHEMKIN package [19, 20] to obtain kinetic rates and thermodynamics properties, a double precision version of the public domain edition of the TRANSPORT package [21] to calculate multi-component transport properties of species, and a double precision version of the public domain edition of the PREMIX algorithm [14] to obtain the steady structure of adiabatic laminar premixed flames.

In this study, the resolved structure is obtained by solving the standard form, Eqs. (2.5)-(2.7), and the eigenvalues are obtained from Eq. (2.16). Most calculations are performed on a uniform grid to enable the grid resolution study. As a check, using a standard option available in PREMIX, some results are obtained on a grid that is *adaptively refined* to control the error and capture regions of steep gradient. A second order central difference scheme is employed to discretize the spatial derivatives. All calculations presented have been performed on a single processor 3.2 GHz Hewlett-Packard machine, and typical calculations were completed within one minute. Some highly resolved calculations done in grid convergence studies required significant run times; the most resolved calculation took several weeks.

3   Results

A stoichiometric hydrogen-air mixture at $p_o = 1$ atm is considered, where the initial molar ratio is given by $2H_2 + O_2 + 3.76N_2$. A kinetic model identical to that of Smooke *et al.* [11], with $L = 3$ elements, $N = 9$ species, and $J = 19$ reversible reactions is used; see Table 1. In this mechanism, the reactant species are $H_2, O_2, H, O, OH, HO_2, H_2O_2$, and H_2O. The inert diluent is N_2. The non-unity coefficients of the collision efficiency of the ith specie with the third body in the jth reaction are listed in Table 2. To verify our predictions, we 1) informally compare our results to those previously reported in the literature and more rigorously examine the finest length scale used in a standard adaptive grid modeling strategy, 2) determine the grid resolution necessary to accurately capture the peak value of a challenging intermediate specie, HO_2, which is most active in the flame zone, 3) perform a formal grid convergence study, and 4) present the results of the spatial eigenvalue analysis and compare the length scale predictions with the direct computational evidence. For all dependent variables z_i, the relative errors, $E_{\infty i}$ throughout the entire domain are obtained from the following formula:

$$E_{\infty i} = \max_{x_o \leq x \leq x_{eq}} \left| \frac{z_i^{exact}(x) - z_i(x)}{z_i^{exact}(x)} \right|. \tag{3.1}$$

Here we take x_o to be the location of the cold boundary and x_{eq} to be the location of the equilibrium state. In practice, both x_o and x_{eq} will be approximated by finite numbers; also, the exact solution for a state variable $z_i^{exact}(x)$ is estimated by a highly refined discrete solution, to be described in more detail in the following sections.

Table 1: Reaction mechanism rate coefficients for hydrogen-air mixture.

j	Reaction	$A_j \left[(\text{mole}/\text{cm}^3)^{\left(1-\sum_{i=1}^{N}\nu'_{ij}\right)}/\text{s}/\text{K}^{\beta_j}\right]$	β_j	E_j [cal/mole]
1	$H_2+O_2 \rightleftharpoons OH+OH$	1.70×10^{13}	0.000	47780
2	$OH+H_2 \rightleftharpoons H_2O+H$	1.17×10^{9}	1.300	3626
3	$H+O_2 \rightleftharpoons OH+O$	5.13×10^{16}	-0.816	16507
4	$O+H_2 \rightleftharpoons OH+H$	1.80×10^{10}	1.000	8826
5	$H+O_2+M \rightleftharpoons HO_2+M$	2.10×10^{18}	-1.000	0
6	$H+O_2+O_2 \rightleftharpoons HO_2+O_2$	6.70×10^{19}	-1.420	0
7	$H+O_2+N_2 \rightleftharpoons HO_2+N_2$	6.70×10^{19}	-1.420	0
8	$OH+HO_2 \rightleftharpoons H_2O+O_2$	5.00×10^{13}	0.000	1000
9	$H+HO_2 \rightleftharpoons OH+OH$	2.50×10^{14}	0.000	1900
10	$O+HO_2 \rightleftharpoons O_2+OH$	4.80×10^{13}	0.000	1000
11	$OH+OH \rightleftharpoons O+H_2O$	6.00×10^{8}	1.300	0
12	$H_2+M \rightleftharpoons H+H+M$	2.23×10^{12}	0.500	92600
13	$O_2+M \rightleftharpoons O+O+M$	1.85×10^{11}	0.500	95560
14	$H+OH+M \rightleftharpoons H_2O+M$	7.50×10^{23}	-2.600	0
15	$H+HO_2 \rightleftharpoons H_2+O_2$	2.50×10^{13}	0.000	700
16	$HO_2+HO_2 \rightleftharpoons H_2O_2+O_2$	2.00×10^{12}	0.000	0
17	$H_2O_2+M \rightleftharpoons OH+OH+M$	1.30×10^{17}	0.000	45500
18	$H_2O_2+H \rightleftharpoons HO_2+H_2$	1.60×10^{12}	0.000	3800
19	$H_2O_2+OH \rightleftharpoons H_2O+HO_2$	1.00×10^{13}	0.000	1800

Table 2: Third body collision efficiency coefficients, α_{ji}. All other values not in the table are 1.

Reaction	H_2	H	H_2O
5	3.3	1	21
12	3	2	6
14	1	1	20

3.1 Adaptive refinement verification

The following calculations use the standard adaptive mesh refinement technique available in the PREMIX code. For informal verification, a calculation is performed to reproduce the temperature and species profiles of the stoichiometric, atmospheric pressure hydrogen-air flame found in Smooke *et al.* [11]. Eqs. (2.5)-(2.7) with the boundary conditions Eqs. (2.8)-(2.10) are solved; this model is identical to that of [11]. The specified spatial point is $x_f = 0.05$ cm, the specified temperature is $T_f = 400$ K, and the temperature of the unburned mixture is $T_o = 298$ K. In this particular calculation, while the Dufour effect in the heat flux model is neglected, the Soret effect in the mass flux model is considered to match the model in [11]. Although considering one of these terms and neglecting the other violates Onsager reciprocity, this is done here for verification purposes only. The results are illustrated in Fig. 1; visual inspection shows that the stationary flame structure
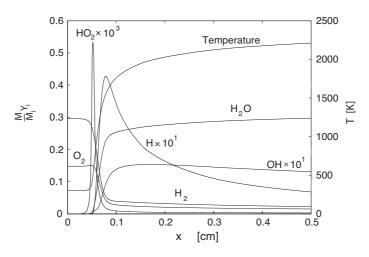
Figure 1: Temperature and species mole fraction ($\chi_i = MY_i/M_i$) profiles vs. distance in a stoichiometric hydrogen-air flame, $T_o = 298$ K, $p_o = 1$ atm.

is identical to that of [11]. To enable direct comparison with [11], we plot mole fraction, $\chi_i = MY_i/M_i$; the remainder of our species profiles which follow are in terms of mass fraction, Y_i.

The predictions shown in Fig. 1 support the standard interpretation of a flame. In short, for small x there is a preheat zone where major species have nearly constant mass fractions. In this zone, minor species have small mass fractions which exhibit exponential growth, though this is not evident on the linear scale of Fig. 1, and the temperature rises slowly. At a certain location within the flame structure, minor species achieve critical values which enable vigorous reaction in what is called the flame zone. Here, some radical species such as HO_2 acquire large, sharply peaked, values relative to their values in the cold and near-equilibrium regions. For larger x, the system relaxes to a final equilibrium. In this region, exothermic recombination reactions dominate as the major product H_2O is formed in large quantities. Though not evident on the linear scale shown in Fig. 1, the solutions are mildly corrupted near the cold boundary $x = 0$, preventing an effective display of flame dynamics in this region. Due to finite double precision machine accuracy, some of the reactive species mass fractions near the cold boundary 1) artificially converge to negative values, and 2) show oscillations. Nevertheless, the behavior away from the cold boundary has no obvious errors.

In order to suppress numerical anomalies near the cold boundary so as to fully expose the behavior in all regions of the flame, the cold boundary temperature is raised to 800 K for our remaining calculations. Fully resolved steady temperature and species profiles for this temperature are shown in Figs. 2 and 3. Although linear scales are usually used in the literature, here log-log and semi-log scales have been employed to better illustrate the disparate scales. Fig. 2 shows the spatial distribution of species mass fractions throughout the entire flame zone. At $x \approx 5 \times 10^{-4}$ cm, the minor species growth
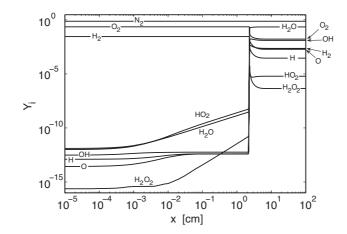
Figure 2: Species mass fraction vs. distance for a stoichiometric hydrogen-air flame, $T_o = 800$ K, $p_o = 1$ atm.
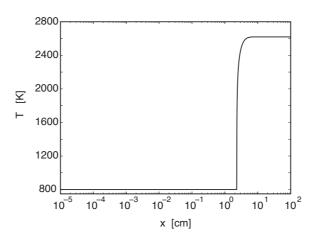

Figure 3: Temperature vs. distance for the stoichiometric hydrogen-air flame, $T_o = 800$ K, $p_o = 1$ atm.

rates change slightly, which reveals that significant dissociation reactions at this scale are induced. Another increase in the minor species mass fraction growth rates is noted at $x \approx 10^{-2}$ cm, which indicates the occurrence of more vigorous chemical interaction of the minor species. For $10^{-2} < x < 2.2 \times 10^0$ cm, the minor species mass fractions continue to increase rapidly with different growth rates. On the other hand, the major species H_2, O_2, and N_2 have essentially constant mass fractions. Just past $x = 2.2 \times 10^0$ cm, which is near the end of the preheat zone, all the species mass fractions undergo significant change, and the radicals' mass fractions reach their maximum values. At $x = 2.4 \times 10^0$ cm, exothermic recombination of radicals commences forming the predominant product H_2O. This zone extends up to $x = 1.4 \times 10^1$ cm; after that, the system comes to an equilibrium where all spatial gradients vanish. To confirm this, the spatial domain is extended to $x = 10^2$ cm, but no further changes are noted.

In Fig. 3, the temperature profile is presented. At $x \approx 2.2 \times 10^0$ cm, the reaction un-

dergoes a particularly vigorous stage in which the change in temperature is significant. Thus, the ignition point can be assigned; it is defined as the point where the temperature gradient dT/dx reaches its maximum value. Also, this particular point defines the end of the preheat zone and the beginning of the reaction zone. For this case the ignition point is assigned at $x = 2.315 \times 10^0$ cm. We adopt the simple estimate for the characteristic reaction length scale (i.e. flame thickness) given by Williams [22], pp. 130-136,

$$\ell_{reaction} = \frac{k}{\rho_o c_p S},\tag{3.2}$$

where for this case $\ell_{reaction} = 1.60 \times 10^{-3}$ cm.

The location of the finest grid predicted by the adaptive refinement algorithm is in fact in the flame zone, near $x = 2.3$ cm, and the resolution necessary to achieve the prescribed error tolerance was $\Delta x = 6 \times 10^{-5}$ cm. Note that this is over an order of magnitude smaller than $\ell_{reaction}$.

3.2   Intermediate species peak capturing verification

The accurate capture of the peak values of species which are highly active only in the flame zone poses a computational challenge. We systematically examine the grid resolution necessary for the precise prediction of one such specie, HO_2. For this, the PREMIX code [14] is now used to obtain solutions over a wide range of *uniform* grid sizes: $3 \times 10^{-2} \le \Delta x \le 6.25 \times 10^{-5}$ cm. Here, the error-control feature in the adaptive refinement algorithm of PREMIX is suppressed to enable these calculations.

Table 3: Peak value of Y_{HO_2} and relative error as functions of Δx.

Δx [cm]	Y_{HO_2}, peak	E_{HO_2}
3.0×10^{-2}	1.33366×10^{-4}	2.23×10^{-1}
1.0×10^{-2}	1.60060×10^{-4}	6.71×10^{-2}
1.0×10^{-3}	1.69659×10^{-4}	1.11×10^{-2}
1.25×10^{-4}	1.71143×10^{-4}	2.47×10^{-3}
6.25×10^{-5}	1.71566×10^{-4}	-

The peak values of Y_{HO_2} as a function of Δx are listed in Table 3. Assuming the value obtained on the finest grid to be "exact" allows calculation of E_{HO_2}; here the calculation of E is restricted to peak values. For coarse grids, there are large relative errors in peak values; the error decreases as the grid size is decreased. We see in Fig. 4 a close view of how the HO_2 mass fraction profile varies with the grid resolution. Fig. 4 does not display the result for $\Delta x = 6.25 \times 10^{-5}$ cm as on this scale it is indistinguishable from that found for $\Delta x = 1.25 \times 10^{-4}$ cm. Clearly the peak, and the behavior near the peak, is under-resolved for $\Delta x \ge 10^{-2}$ cm. Most of the structure near the peak is well resolved for $\Delta x = 10^{-3}$ cm; for $\Delta x = 1.25 \times 10^{-4}$ cm, the error is very small; $E_{HO_2} = 2.47 \times 10^{-3}$.
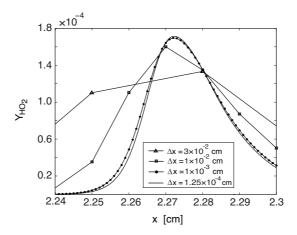
Figure 4: Magnified view of Y_{HO_2} vs. x for various uniform values of Δx for the hydrogen-air flame simulation with $T_o = 800$ K and $p_o = 1$ atm.
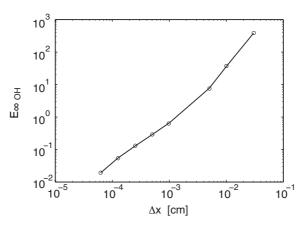

Figure 5: Relative error of Y_{OH} vs. the discretization size for the hydrogen-air flame simulation with $T_o = 800$ K and $p_o = 1$ atm.

3.3 Grid convergence verification

While correct capture of peak values of challenging species is a necessary condition for grid resolution, a more systematic and rigorous verification is given by a formal grid convergence study, which is reported next. The result for one dependent variable, Y_{OH}, is presented in Fig. 5. Results for all other variables bear remarkable similarity to that for Y_{OH}, and so are not presented here. Solutions are obtained on eight different uniform grids. The "exact" solution is estimated using Richardson's extrapolation from the three finest grids [1]. In computing the error via Eq. (3.1), points with species mole fraction below 10^{-10} were excluded because of potential roundoff corruption in the double precision calculations.

Fig. 5 shows that to obtain a desirable $E_{\infty OH} < 0.1$ in this problem, a spatial resolution of $\Delta x \leq 2 \times 10^{-4}$ cm has to be utilized. Larger grid sizes can induce unacceptably large

relative errors; e.g. for $\Delta x = 10^{-2}$ cm the relative error in Y_{OH} is 40! In addition, it is found that the error at the finest two spatial discretizations is converging towards the exact solution at a rate of $\mathcal{O}(\Delta x^{1.64})$. It appears in Fig. 5 that the rate of convergence is increasing as Δx decreases. Finite computational resources prevented the use of finer grids; it is expected that on even finer grids, a convergence rate of $\mathcal{O}(\Delta x^2)$, consistent with the truncation error of the finite difference discretization, would have been achieved.

Consideration of the spatial distribution of Y_{OH} at four different grid resolutions, shown in Fig. 6, provides additional insight. Here, attention is focused on a region at the onset of flame ignition. Clearly one sees that for $\Delta x = 3 \times 10^{-2}$ cm and 1×10^{-2} cm, relative to calculations on a finer grid, there are orders of magnitude difference in the predictions of Y_{OH}. Only for the finer grid resolution is Y_{OH} seen to be converging to achieve a small relative error.
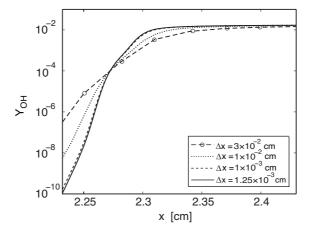

Figure 6: Spatial distribution of Y_{OH} at various discretization sizes for the hydrogen-air flame simulation with $T_o = 800$ K and $p_o = 1$ atm.

In contrast, for this problem, the relative errors in laminar flame speed are not as sensitive. Fig. 7 shows the relative error in laminar flame speed $(S - S_e)/S_e$ as a function of Δx, where S_e is the approximation to the exact laminar flame speed found from Richardson extrapolation from the three finest grids. To keep the relative error in S below 0.1, one need only employ a $\Delta x \sim 2 \times 10^{-3}$ cm. For $\Delta x = 10^{-2}$ cm, the relative error in S is approximately 0.4, much smaller than that for species mass fractions.

3.4 Spatial eigenvalue analysis verification

Having the fully resolved structure in hand, the local Jacobian and the spatial generalized eigenvalues are calculated from the cold boundary to near equilibrium. As a result, the local length scales ℓ_i are predicted throughout the domain; these results are shown in Fig. 8. The multi-scale nature of the problem and the length scales over which the species evolve are clearly shown. The finest length scale and the largest length scale for this
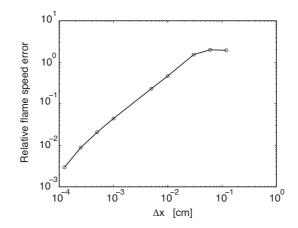
Figure 7: Convergence of the relative error in laminar flame speed, $(S-S_e)/S_e$ with grid size Δx for the hydrogen-air flame simulation with $T_o=800$ K and $p_o=1$ atm.
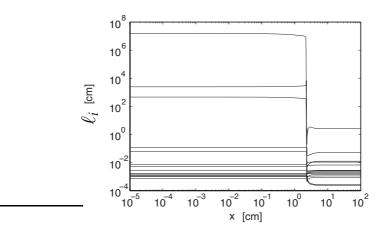

Figure 8: Predicted length scales over which stoichiometric hydrogen-air flame evolve vs. distance, $T_o=800$ K, $p_o=1$ atm.

system vary from 7.60×10^{-4} cm and 1.62×10^7 cm in the preheat zone to 2.41×10^{-4} cm and 2.62×10^0 cm in the reaction zone, respectively.

The evolution of a particular specie is not associated with a particular length scale, since the species mass fractions depend on local linear combinations of all eigenmodes. So, the species mass fractions can vary on these scales through the entire domain. The finest scale in the preheat zone, $\sim10^{-3}$ cm, is a good predictor of when significant variation of minor species is exhibited, although the variations are very small. In the preheat zone, $x<2$ cm, the scales are all relatively invariant with x. This is likely because the major species and many minor species themselves exhibit little variation in this region. Slight changes are mainly a consequence of the growth of minor species such as HO_2 and H_2O_2. At the beginning of the flame zone, near $x\sim2$ cm, the finest length scale begins to drop to $\sim10^{-4}$ cm. It is in this region that there are many active growing modes, as

reflected for example in the local peaks of HO_2 studied earlier. As the flame relaxes to equilibrium at $x \sim 10$ cm, the finest scale relaxes. Here it is likely that such fine scales are associated with decaying modes, as there are no fine scale structures evident in the final relaxation towards equilibrium. As the system approaches equilibrium, all of the eigenvalues are real: half are positive, and half are negative. Thus, the equilibrium point is a high order saddle node.

We note that the spatial eigenvalue analysis gives results consistent with the detailed grid convergence analysis. The eigenvalue analysis is potentially more conservative than the grid convergence study since some or many eigenmodes associated with fine scale eigenvalues may in fact be of negligible amplitude. This is likely the case on the approach to equilibrium, but not the case in the flame zone. In any case, the grid convergence study is comprehensive in that it reflects the magnitude of *all* modes. Since the detailed spatial profiles reveal that the largest resolution errors reside in the flame zone, we speculate that it is in this region that the spatial eigenvalues give the best estimate of where the finest resolution is required.
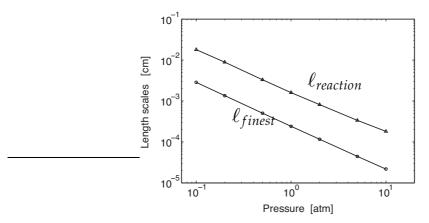

Figure 9: The flame thickness and the finest length scale predicted by eigenvalue analysis vs. pressure for stoichiometric hydrogen-air flame, $T_o = 800$ K.

Following the same procedure, a comparison between the predicted finest length scale ℓ_{finest} and the flame thickness $\ell_{reaction}$ over a wide range of pressures is presented in Fig. 9. The figure reveals that the finest length scale is well correlated with the flame thickness and that both decrease as pressure is increased. On the other hand, ℓ_{finest} is at least one order of magnitude smaller than $\ell_{reaction}$, which indicates the presence of reaction-induced scales smaller than the flame thickness.

The present approach has been extended to several other stoichiometric mixtures [23]: 1) methane-air, 2) ethane-air, 3) propane-air, 4) ethylene-air, and 5) acetylene-air. The GRI 3.0 mechanism [24] with $L = 5$ elements, $N = 53$ species, and $J = 325$ reversible reactions was adopted as a kinetic model. For each mixture, two cases were studied: 1) the freely propagating laminar flame, and 2) the Chapman-Jouguet detonation. Results in all cases were consistent with those presented for hydrogen-air mixtures.

4   Conclusions

One-dimensional steady calculations reveal that for an adiabatic laminar premixed flame freely propagating in stoichiometric hydrogen-air mixtures described by detailed kinetics and multi-component transport, the required grid resolution to formally resolve all modeled flow structures, including detailed species mass fractions, is at the micron-level for flames at atmospheric pressure. The requirements are less stringent if one seeks only to correctly capture such macro-features as flame speed and equilibrium properties. However, it should be noted that employing a grid on which the flame speed or other derived quantity is grid-insensitive does not guarantee that detailed species mass fractions are grid-insensitive.

The micron length scale has been predicted by an adaptive refinement algorithm, analysis of the peak values of intermediate species in the flame zone, a formal grid convergence study, and detailed spatial eigenvalue analysis. The length scale predictions are fully reflective of the underlying physics of advection and diffusion coupled with detailed kinetics, and not the particular numerical method chosen. The implications for future calculations of challenging combustion dynamics remain to be seen, but it is likely that proper accounting of commonly modeled state variables gives rise to more stringent computational grid requirements than are commonly employed.

Acknowledgments

Appendix

A.1   Constitutive relations

The system of equations, (2.1)-(2.4), is completed by adopting the following constitutive relations:

$$J_i^m = \rho \sum_{\substack{k=1 \\ k \neq i}}^{N} \frac{M_i D_{ik} Y_k}{M} \left(\frac{1}{\chi_k} \frac{\partial \chi_k}{\partial \tilde{x}} + \left(1 - \frac{M_k}{M} \right) \frac{1}{p} \frac{\partial p}{\partial \tilde{x}} \right) - D_i^T \frac{1}{T} \frac{\partial T}{\partial \tilde{x}}, \quad 1 \leq i \leq N-1, \qquad \text{(A.1)}$$

$$J^q = q + \sum_{i=1}^{N} J_i^m h_i - \Re T \sum_{i=1}^{N} \frac{D_i^T}{M_i} \left(\frac{1}{\chi_i} \frac{\partial \chi_i}{\partial \tilde{x}} + \left(1 - \frac{M_i}{M} \right) \frac{1}{p} \frac{\partial p}{\partial \tilde{x}} \right), \qquad \text{(A.2)}$$

$$q = -k \frac{\partial T}{\partial \tilde{x}}, \quad p = \Re T \sum_{i=1}^{N} \bar{\rho}_i, \quad e = h - \frac{p}{\rho}, \qquad \text{(A.3)}$$

$$1 = \sum_{i=1}^{N} Y_i, \quad 1 = \sum_{l=1}^{L} Y_l^e, \quad 0 = \sum_{i=1}^{N} J_i^m, \quad 0 = \sum_{l=1}^{L} J_l^e, \tag{A.4}$$

$$\dot{\omega}_i = \sum_{j=1}^{J} \nu_{ij} r_j, \quad 1 \le i \le N, \tag{A.5}$$

$$r_j = k_j \left(\prod_{i=1}^{N} (\bar{\rho}_i)^{\nu'_{ij}} - \frac{1}{K_j^c} \prod_{i=1}^{N} (\bar{\rho}_i)^{\nu''_{ij}} \right), \quad 1 \le j \le J, \tag{A.6}$$

$$k_j = A_j \, T^{\beta_j} \exp \left(\frac{-E_j}{\Re T} \right), \quad 1 \le j \le J, \tag{A.7}$$

$$K_j^c = \left(\frac{p^{ref}}{\Re T} \right)^{\sum_{i=1}^{N} \nu_{ij}} \exp \left(-\frac{\sum_{i=1}^{N} \bar{\mu}_i^o \nu_{ij}}{\Re T} \right), \quad 1 \le j \le J, \tag{A.8}$$

$$\bar{\rho}_{M_j} = \sum_{i=1}^{N} \alpha_{ji} \bar{\rho}_i, \quad 1 \le j \le J, \tag{A.9}$$

$$h_i = h_i^f + \int_{T^{ref}}^{T} c_{pi}(\tilde{T}) d\tilde{T}, \quad 1 \le i \le N, \tag{A.10}$$

$$s_i^o = s_i^f + \int_{T^{ref}}^{T} \frac{c_{pi}}{\tilde{T}} d\tilde{T}, \quad \bar{\mu}_i^o = M_i (h_i - T s_i^o), \quad 1 \le i \le N, \tag{A.11}$$

$$h = \sum_{i=1}^{N} Y_i h_i, \quad c_p = \sum_{i=1}^{N} Y_i c_{pi}, \quad M = \left(\sum_{i=1}^{N} \frac{Y_i}{M_i} \right)^{-1}, \tag{A.12}$$

$$\chi_i = \frac{M}{M_i} Y_i, \quad \bar{\rho}_i = \frac{\rho Y_i}{M_i}, \quad M_i = \sum_{l=1}^{L} m_l \phi_{li}, \quad 1 \le i \le N, \tag{A.13}$$

$$\nu_{ij} = \nu''_{ij} - \nu'_{ij}, \quad 1 \le i \le N, \quad 1 \le j \le J, \tag{A.14}$$

$$0 = \sum_{i=1}^{N} \phi_{li} \nu_{ij}, \quad 1 \le j \le J, \quad 1 \le l \le L, \tag{A.15}$$

$$Y_l^e = m_l \sum_{i=1}^{N} \frac{\phi_{li} Y_i}{M_i}, \quad J_l^e = m_l \sum_{i=1}^{N} \frac{\phi_{li} J_i^m}{M_i}, \quad 1 \le l \le L, \tag{A.16}$$

$$c_{pi} = \frac{\Re}{M_i} \left(a_{1i} + a_{2i} T + a_{3i} T^2 + a_{4i} T^3 + a_{5i} T^4 \right), \quad 1 \le i \le N, \tag{A.17}$$

$$h_i^f = \frac{\Re}{M_i} \left(a_{1i} T + \frac{a_{2i}}{2} T^2 + \frac{a_{3i}}{3} T^3 + \frac{a_{4i}}{4} T^4 + \frac{a_{5i}}{5} T^5 + a_{6i} \right), \quad 1 \le i \le N, \tag{A.18}$$

$$s_i^f = \frac{\Re}{M_i} \left(a_{1i} \ln(T) + a_{2i} T + \frac{a_{3i}}{2} T^2 + \frac{a_{4i}}{3} T^3 + \frac{a_{5i}}{4} T^4 + a_{7i} \right), \quad 1 \le i \le N. \tag{A.19}$$

In Eqs. (A.1)-(A.19), the dependent variables are mixture-average molecular mass M, Fourier heat flux q, mass-based specific enthalpy of the mixture h, and for the ith specie, $\chi_i, \bar{\rho}_i, c_{pi}, s_i^o$, and $\bar{\mu}_i^o$, which are the mole fraction, the molar concentration (i.e. molar density), mass-based specific heat at constant pressure, mass-based specific enthalpy, mass-

based specific entropy at standard pressure, and molar-basis specific chemical potential, respectively. For each reaction from $j = 1, \cdots, J$, the new variables are r_j, k_j, and K_j^c, which denote the reaction rate, the temperature-dependent Arrhenius coefficient, and the equilibrium constant, respectively. For the lth element, Y_l^e and J_l^e are the element mass fraction and element mass flux. The variables D_{ik}, k, and D_i^T are the multi-component diffusion coefficients, the temperature-dependent mixture thermal conductivity, and the thermal diffusion coefficient of specie i, where these three variables are computed from the solution of the detailed L-matrix system given by Dixon-Lewis [25]; due to extreme length, details are omitted here. The constant parameters are the universal gas constant $\Re = 8.314 \times 10^7$ erg mole^{-1} K^{-1}, the reference pressure $p^{ref} = 1$ atm, and the reference temperature $T^{ref} = 298$ K. For the ith specie $h_i^f, s_i^f, a_{1i}, \cdots, a_{7i}$ denote the mass-based specific enthalpy of formation, the reference state mass-based specific entropy, and the coefficients of the curve fit for c_{pi}, h_i^f, and s_i^f which can be found in [20]. For each reaction from $j = 1, \cdots, J$, we have $A_j, \beta_j, E_j, v_{ij}'', v_{ij}'$, and v_{ij} which represent the collision frequency factor, the temperature-dependency exponent, the activation energy, the stoichiometric coefficient of specie i denoting the number of moles of reactants and products, and the net stoichiometric coefficient, respectively. Moreover, for the jth reaction $\bar{\rho}_{M_j}$ and α_{ji} are the third body molar concentration and the coefficients of the collision efficiency of the ith specie with the third body, where these coefficients play a role only in the reactions that contain a third body. In addition, for each element from $l = 1, \cdots, L$, m_l denotes the element mass and ϕ_{li} the element index of specie i, which gives the number of moles of element l in specie i.

Eqs. (A.1)-(A.2) are appropriate for a mixture of ideal gases [26], and describe multi-component mass diffusion fluxes including the Soret effect, and the heat flux including the Dufour effect. Eq. (A.3) defines Fourier's law, the thermal state equation for an ideal gas mixture, and the definition of enthalpy, respectively. Eq. (A.4) constrains the species and element mass fractions as well as species and element mass fluxes to sum to unity and zero, respectively. Eqs. (A.5)-(A.8) are expressions of the molar species evolution rate per unit volume of specie i, the law of mass action, the Arrhenius reaction rate, and the equilibrium constant, respectively. Eq. (A.9) is an expression for the third body molar concentration in reaction j. Eqs. (A.10)-(A.11) define the temperature-dependent enthalpy, entropy, and chemical potential for specie i at the reference pressure, respectively. Eq. (A.12) gives mixture rules for mixture mass-based specific enthalpy and heat, and the mixture-averaged molecular mass. Eqs. (A.13)-(A.14) define the mole fraction of specie i, the molar concentration of specie i, the molecular mass of specie i, and the net stoichiometric coefficients, respectively. Eq. (A.15) is a stoichiometric constraint on element l in reaction j which represents a mass balance for each element. Eq. (A.16) defines the element mass fraction and flux. Finally, Eqs. (A.17)-(A.19) are curve fits of c_{pi}, h_i^f, and s_i^f. Formally, to complete the system, one must also consider a constitutive equation for the stress, such as $\tau = (4/3)\mu(\partial \tilde{u}/\partial \tilde{x})$, where μ is the first viscosity coefficient; this does not play a role in our analysis.

A.2   Dynamical system model equations

We describe here the reductions necessary to arrive at a set of DAEs to describe the flame structure. The complete system of PDEs, Eqs. (2.1)-(2.4), is first reduced into a system of ordinary differential equations (ODEs) by relaxing the time-dependent behavior of the system to a steadily propagating flame front with constant, albeit unknown, flame speed S. A Galilean transformation is applied to the system with the frame speed equal to the flame speed,

$$x = \tilde{x} + S\tilde{t}, \tag{A.20a}$$

$$t = \tilde{t}, \tag{A.20b}$$

$$u = \tilde{u} + S. \tag{A.20c}$$

The spatial coordinate x is a flame front-attached coordinate, and u is the mixture velocity in the flame frame. Consequently, the equations that govern the structure of a steady flame are obtained, where after employing the third equation in Eq. (A.3) and standard manipulations they become, in a non-conservative form,

$$\frac{d}{dx}(\rho u) = 0, \tag{A.21a}$$

$$\rho u \frac{du}{dx} + \frac{dp}{dx} - \frac{d\tau}{dx} = 0, \tag{A.21b}$$

$$\rho u \frac{dh}{dx} + \frac{dJ^q}{dx} - u\frac{dp}{dx} - \tau\frac{du}{dx} = 0, \tag{A.21c}$$

$$\rho u \frac{dY_i}{dx} + \frac{dJ_i^m}{dx} = \dot{\omega}_i M_i, \quad 1 \leq i \leq N-1. \tag{A.21d}$$

At this point, the low-Mach number assumption is adopted, which has the consequence of rendering the thermodynamic pressure constant and suppressing the viscous dissipation and the advection of pressure in Eq. (A.21c). This assumption is reasonable for deflagration [22], and implies that for a fixed mass flux the momentum equation no longer need be considered. Subsequently, all the thermodynamic properties, throughout the reaction zone, are evaluated at the surrounding thermodynamic pressure, p_o. Eqs. (2.5)-(2.7) are obtained by employing Eqs. (A.21a) and (A.21d), substituting Eqs. (A.2), (A.10), and the first equation in (A.12) into Eq. (A.21c), and neglecting the Dufour effect, following the same approach as in Aris [27]. Returning to Eq. (A.21), if we multiply the evolution of species, Eq. (A.21d), with $m_l \phi_{li}$, sum from $i = 1$ to N, and employ Eqs. (A.5), (A.15)-(A.16), and (A.21a), the governing equations are recast in a conservative form by adding Eq. (A.21a) to Eqs. (A.21c)-(A.21d):

$$\frac{d}{dx}(\rho u) = 0, \tag{A.22a}$$

$$\frac{d}{dx}(\rho u h + J^q) = 0, \tag{A.22b}$$

$$\frac{d}{dx}(\rho u Y_l^e + J_l^e) = 0, \qquad 1 \leq l \leq L-1, \tag{A.22c}$$

$$\frac{d}{dx}(\rho u Y_i + J_i^m) = \dot{\omega}_i M_i, \quad 1 \leq i \leq N-L. \tag{A.22d}$$

This system of ODEs, describing the steadily propagating laminar premixed flame, consists of $N+1$ equations. These are supplemented by the N ODEs embodied in Eqs. (A.1)-(A.3), forming a total of $2N+1$ ODEs. Thus the $2N+1$ boundary conditions of Eqs. (2.8)-(2.10) are required.

It is useful to have additional values of variables at boundaries. Using Eqs. (A.3), (A.10), (A.12), and (A.16) the following expressions are derived

$$\rho_o = \frac{p_o}{\Re T_o \sum_{i=1}^{N} \frac{Y_{io}}{M_i}}, \tag{A.23a}$$

$$h_o = \sum_{i=1}^{N} Y_{io} \left(h_i^f + \int_{T^{ref}}^{T_o} c_{pi}(\tilde{T}) d\tilde{T} \right), \tag{A.23b}$$

$$Y_{lo}^e = m_l \sum_{i=1}^{N} \frac{\phi_{li} Y_{io}}{M_i}, \quad 1 \leq l \leq L. \tag{A.23c}$$

By utilizing the boundary conditions (A.23), the homogeneous ODEs, Eq. (A.22), can be integrated exactly. Subsequently, the governing equations become

$$\rho u = \rho_o S, \tag{A.24a}$$

$$\rho_o S h + J^q = \rho_o S h_o, \tag{A.24b}$$

$$\rho_o S Y_l^e + J_l^e = \rho_o S Y_{lo}^e, \qquad 1 \leq l \leq L-1, \tag{A.24c}$$

$$\frac{d}{dx}(\rho_o S Y_i + J_i^m) = \dot{\omega}_i M_i, \quad 1 \leq i \leq N-L. \tag{A.24d}$$

At this stage the variable S is considered a fixed parameter for a given calculation; an iterative technique is used to determine S so that all boundary conditions are satisfied. The equations are most conveniently posed as a set of $2N+2$ DAEs in terms of $2N+2$ state variables; specie mass fraction Y_i, $(i=1,\cdots,N)$, specie mass flux J_i^m, $(i=1,\cdots,N)$, temperature T, and Fourier's heat flux q. This system, in a compact representation, is

$$\mathbf{A} \cdot \frac{d\mathbf{z}}{dx} = \mathbf{f}, \tag{A.25}$$

where

$$
\mathbf{A} =
\begin{bmatrix}
\mathcal{D} & \mathbf{0} & \mathbf{0} \\
\dot{\mathcal{M}} & \mathcal{I} & \mathbf{0} \\
\mathbf{0} & \mathbf{0} & \mathcal{Q}
\end{bmatrix},
\quad
\mathbf{z} =
\begin{bmatrix}
Y_1 \\
\vdots \\
Y_N \\
J_1^m \\
\vdots \\
J_N^m \\
T \\
q
\end{bmatrix},
\quad
\mathbf{f} =
\begin{bmatrix}
\frac{J_1^m M}{\rho M_1} \\
\vdots \\
\frac{J_N^m M}{\rho M_N} \\
\dot{\omega}_1 M_1 \\
\vdots \\
\dot{\omega}_{N-L} M_{N-L} \\
\rho u Y_1^e + J_1^e - (\rho_o S Y_{1o}^e) \\
\vdots \\
\rho u Y_L^e + J_L^e - (\rho_o S Y_{Lo}^e) \\
\rho u h + J^q - (\rho_o S h_o) \\
q
\end{bmatrix},
\tag{A.26}
$$

with

$$
\mathcal{D} = D_{ik} - \sum_{\substack{m=1 \\ m \neq i}}^{N} \frac{D_{im} Y_m M}{M_k}, \qquad 1 \leq i,k \leq N, \tag{A.27a}
$$

$$
\dot{\mathcal{M}} = \left[- - \frac{\rho_o S \mathbf{I}_{(N-L) \times (N-L)}}{\mathbf{0}_{L \times (N-L)}} \; \vdots \; \frac{\mathbf{0}_{(N-L) \times L}}{\mathbf{0}_{L \times L}} - - \right], \tag{A.27b}
$$

$$
\mathcal{I} = \left[- - \frac{\mathbf{I}_{(N-L) \times (N-L)}}{\mathbf{0}_{L \times (N-L)}} \; \vdots \; \frac{\mathbf{0}_{(N-L) \times L}}{\mathbf{0}_{L \times L}} - - \right], \tag{A.27c}
$$

$$
\mathcal{Q} =
\begin{bmatrix}
0 & 0 \\
-k & 0
\end{bmatrix}. \tag{A.27d}
$$

Note that **A** is a singular matrix of dimension $(2N+2) \times (2N+2)$ with rank of $2N-L$, **f** is a set of $(2N+2) \times 1$ non-linear functions of the state variables **z**, also of dimension $(2N+2) \times 1$, and **I** is the identity matrix. Here, the dimensions of $\mathcal{D}, \dot{\mathcal{M}}$, and $\mathcal{I}$ are $N \times N$, while the dimension of $\mathcal{Q}$ is 2×2.

The dynamical system (A.25) is useful for length scale analysis via generalized eigenvalues. Direct solution of this system for the reaction zone structure is possible, in principle. However, the problem can be shown to be a high order shooting problem, rendering direct solution difficult.

References

[1] P. J. Roache, Quantification of uncertainty in computational fluid dynamics, Annu. Rev. Fluid Mech., 29 (1997), 123-160.

[2] J. Stoer and R. Bulirsch, Introduction to Numerical Analysis, Springer-Verlag, Berlin, 2004.

[3] R. D. Richtmyer and K. W. Morton, Difference Methods for Initial-Value Problems, Krieger, Malabar, FL, 1994.

[4] R. J. LeVeque, Finite Volume Methods for Hyperbolic Problems, Cambridge University Press, Cambridge, 151-156, 2002.

[5] A. Iserles, A First Course in the Numerical Analysis of Differential Equations, Cambridge University Press, Cambridge, 2002.

[6] C. J. Roy, Review of code and solution verification procedures for computational simulation, J. Comput. Phys., 205 (2005), 131-156.

[7] W. L. Oberkampf and T. G. Trucano, T. G., Verification and validation in computational fluid dynamics, Prog. Aerosp. Sci., 38 (2002), 209-272.

[8] J. M. Powers and S. Paolucci, Accurate spatial resolution estimates for reactive supersonic flow with detailed chemistry, AIAA J., 43 (2005), 1088-1099.

[9] A. N. Al-Khateeb and J. M. Powers, Verified computations of laminar premixed flames, AIAA-2007-0381, 45th AIAA Aerospace Sciences Meeting and Exhibit, Reno, NV, 2007.

[10] A. N. Al-Khateeb, J. M. Powers, and S. Paolucci, On numerical resolution requirements in combustion modeling, IMECE 2007-42984, ASME International Mechanical Engineering Congress and Exposition, Seattle, WA, 2007.

[11] M. D. Smooke, J. A. Miller, and R. J. Kee, Determination of adiabatic flame speeds by boundary value methods, Combust. Sci. Technol., 34 (1983), 79-90.

[12] R. B. Bird, W. E. Stewart, and E. N. Lightfoot, Transport Phenomena, John Wiley & Sons, New York, NY, 1960.

[13] S. Singh, Y. Rastigejev, S. Paolucci, and J. M. Powers, Viscous detonation in H_2–O_2–Ar using intrinsic low-dimensional manifolds and wavelet adaptive multilevel representation, Combust. Theor. Model., 5 (2001), 163-184.

[14] R. J. Kee, J. F. Grcar, M. D. Smooke, and J. A. Miller, A Fortran Program for Modeling Steady Laminar One Dimensional Premixed Flames, Report No. SAND85–8240, Sandia National Laboratories, Livermore, CA, 1992.

[15] R. J. Kee, M. E. Coltrin, and P. Glarborg, Chemically Reactive Flow: Theory and Practice, Wiley, Hoboken, NJ, 2003.

[16] J. A. Miller, M. D. Smooke, R. M. Green, and R. J. Kee, Kinetic modeling of the oxidation of ammonia in flames, Combust. Sci. Technol., 34 (1983), 149-176.

[17] R. J. Kee and J. A. Miller, Computational modeling of flame structure, Physica D, 12 (1984), 198-211.

[18] G. H. Golub and C. F. Van Loan, Matrix Computations, Johns Hopkins, Baltimore, MD, 1983.

[19] R. J. Kee, F. M. Rupley, and J. A. Miller, Chemkin-II: A Fortran Chemical Kinetics Package for the Analysis of Gas Phase Chemical Kinetics, Report No. SAND89-8009B, Sandia National Laboratories, Livermore, CA, 1992.

[20] R. J. Kee, F. M. Rupley, and J. A. Miller, The Chemkin Thermodynamic Data Base, Report No. SAND87-8215B, Sandia National Laboratories, Livermore, CA, 1992.

[21] R. J Kee, G. Dixon-Lewis, J. Warnatz, M. E. Coltrin, and J. A. Miller, A Fortran Computer Code Package for the Evaluation of Gas-Phase Multicomponent Transport Properties, Report No. SAND86-8246, Sandia National Laboratories, Livermore, CA, 1991.

[22] F. A. Williams, Combustion Theory, Addison-Wesley, Redwood City, CA, 1985.

[23] A. N. Al-Khateeb, J. M. Powers, and S. Paolucci, Length Scale Issues in Combustion Modeling, Technical Report No. 2009-AME-01, University of Notre Dame, Notre Dame, IN, 2009.

[24] G. P. Smith, D. M. Golden, M. Frenklach, N. W. Moriarty, B. Eiteneer, M. Goldenberg, C.

     T. Bowman, R. K. Hanson, S. Song, W. C. Gardiner, V. V. Lissianski, and Z. Qin, GRI-Mech
     3.0, available on line at: `http://www.me.berkeley.edu/gri_mech/` (accessed 8 July 2009).
[25] G. Dixon-Lewis, Flame structure and flame reaction kinetics. II. Transport phenomena in
     multicomponent systems, Proc. Roy. Soc. London A, 307 (1968), 111-135.
[26] H. J. Merk, The macroscopic equations for simultaneous heat and mass transfer in isotropic,
     continuous and closed systems, Appl. Sci. Res. A, 8 (1959), 73-99.
[27] R. Aris, Vectors, Tensors, and the Basic Equations of Fluid Mechanics, Dover, New York, NY,
     1989.